

Controllable bipolaron formation unveiling structural features of trap states in organic charge transport

Zichen Wang¹, Ilia Kulikov², Tarig Mustafa¹, Jan Behrends², Henning Sirringhaus^{1*}

1. Optoelectronics Group, Cavendish Laboratory, University of Cambridge, JJ Thomson Avenue, Cambridge CB3 0HE, UK

2. Berlin Joint EPR Lab, Freie Universität Berlin, Fachbereich Physik, Arnimallee 14, D-14195 Berlin, Germany

*hs220@cam.ac.uk

Abstract

Magnetic resonance methods offer a unique chance for in-depth study of conductive organic material systems, not only accounts for number of charge carriers, but also allows manipulations of spin dynamics of particles. Here we present a study of continuous-wave electrically detected magnetic resonance on a range of organic conjugate polymers under transistor architecture, with tunability in both carrier concentration and drifting electric field. We demonstrate the general existence of bipolaron between mobile and trapped charges at the magnetic resonance condition, then estimates the wavefunction expansion of charge carriers on their hopping sites along conductive pathways. This finding allows direct observation of energetically disordered trap sites under the “charge hopping” picture, linking-up the microscopic structural properties to the bulk electronic performances.

Main Text

Electron spin resonance (ESR) is a new emerging technique in the study of spin-selective exciton and polaron dynamics in organic semiconductors, showing details about spin relaxation and dephasing of (quasi)particles in a chemical environment with neglectable spin-orbital coupling and hyperfine interactions¹⁻⁴. Despite the ESR spectrum holds abundant information of local chemical environments experienced by mobile charges in the disordered systems, the relationship with the charge transport processes remains unclear⁵. In principle spin states of carrier could be used as a probe of scattering process in charge motion, however previous work from S Schott et al. suggests the scattering of carrier spin is complicated local spin density oscillations at increased temperature above 200K¹.

In this paper, we perform a continuous-wave electrically detected magnetic resonance (cw-EDMR) experiment on a planar organic field effect transistor (FET) structure. The FET structure enables a conductive channel with single type of carrier in intrinsic material, where the carrier density and the drift voltage are controlled by external circuits. Different from the widely acknowledged EDMR signal contribution of spin flip between triplet results in a singlet and hence approval of a direct recombination, we are able to prove the existence of a second contribution of EDMR signals - the blocking effects from bipolaron states within the traps on certain percolation paths⁶. We repeat the experiment on various stereotype materials and showing the generality of this phenomenon. Through a temperature sweep measurement, we extract the energy level difference between singlet and triplet states of the bipolaron and evaluate the physical size of the trap sites. Our findings suggest the new opportunity to evaluate the influence of traps states in charge transport processes for wide range of optoelectronic and flexible electronic applications⁷.

The principle of a cw-EDMR measurement is similar to those of ESR: with the presence of a uniform DC magnetic field B_0 and a continuous-wave microwave field at specific frequency, spin states of carriers are excited to resonant between the Zeeman-split energy levels between 2 spin states. Rather than measuring the absorption of the magnetic field at resonance in ESR, the current flowing through the device is monitored as the field swept in EDMR, reflecting a change in current due to a changing spin population. A lock-in detection mode is applied to achieve sensitive detection: a small AC modulation of B_0 is applied, causing the monitored signal response in a periodic pattern, then the mixing of modulation signal picks up the first derivative of the response function. In this paper, we keep a consistent notation of δI_{EDMR} as the measured EDMR spectrum (the unit is in a.u.), and ΔI proportional to integral of δI_{EDMR} as the change of current in the real response function (unit in A). The method to calibrate the measured current is provided in Supplementary Information Section 4. As shown in Figure 1 (a), a top-gated-bottom-contact FET was placed in cavity. The biasing condition

is provided externally, and current flowing through source and drain I_D is monitored with AC components fed into the ESR analyser after amplified. The gate leakage current is kept 1 order smaller than I_D current (supplementary information Section 1), so that the whole system can be modelled as an isolated conductive channel.

Results

Electrical detected magnetic resonance in ambipolar organic transistors

From the starting point, the device is cooled down to 200K for the ESR and EDMR measurements to observe a clear signal free from thermal noise, which will enable a wide range variation of FET bias conditions for the study of the origin of the signal. Poly[2,5-(2-octyldodecyl)-3,6-diketopyrrolopyrrole-alt-5,5-(2,5-di(thien-2-yl)thieno[3,2-b]thiophene)] (DPP-DTT) is selected as the stereotype material throughout the experiment. DPP-based polymer is a series of widely investigated donor-acceptor copolymer with high performance in charge transport and are typically used in OFETs⁸. In particular, DPP-DTT is reported with balanced p and n type performances in single device⁹, making it favourable in the study of the polaron dynamics independent of the carrier types. The spin coated DPPD-TT FET devices exhibit a balanced p and n type performance from 200K to room temperature (shown in Figure 1 (b)), making it a suitable platform to study mechanism of charge transport independent of the nature of the charge carriers. As conjugated polymer transistors suffer from degradation with continuous applied voltages, we apply 1hour recover time and proves that this will make sure we are measure at same conditions (supplementary information Section 2).

At 200K, both ESR and EDMR signals are recorded from both p and n type (shown in Figure 1 (c) (d)). Biased in linear region, the ESR peak has a linear dependence on the gate voltage. The spin concentration is in the order of $10^{19}cm^{-3}$, matched with the value calculated from dielectric measurements (Supplementary information Section 1). No difference in the peak position is observed, whereas the peak amplitudes of the holes are slightly larger than the electrons. These observations show good agreement with our previous observations¹⁰. Therefore, the spin states of the gate-induced charges are processing under the microwave at resonance condition, and the observed EDMR signal reflects the spin dynamics of the mobile charge.

Spin blocking with the formation of bipolarons

To investigate the origin of the EDMR signal, a complete set of scans covering all FET operation regions is performed (illustrated in Figure 2 (a)). In linear regime, the V_{DS} starts at -15V to obtain enough I_D and avoid the I_D nonlinear behaviour near $V_{GS} = -40V$, which is also presented in Chen Z. et al. work⁹, probably due to the contact resistance between DPPDTT material and the gold electrodes without O₂ plasma cleaning. With the varying I_D is varying at each scanning point, normalized $\Delta I/I_D$ indicates the portion of charge carriers undergoing the processes excited at resonance.

Figure 2 (b) sums the $\Delta I/I_D$ results we observed in a wide range of scanning. The total 2D area could be divide into 2 area – linear and saturation region with a gradual variation, and the ambipolar region with a reverse peak. We first focus on the linear and saturation region, following representative black routine ordered in (i) (ii) and (iii) (Figure 2 (c) (d)). In linear region shown in (i), $\Delta I/I_D$ decreases monotonically with the increasing $|V_{GS}|$. Same trend is observed in saturation region where $|V_{GS}|$ increases from 50V to 80V. When the FET working condition shifts from saturation region to the linear region, the signal shows a decrease in amplitude with the increase in drifting voltage $|V_{DS}|$ alongside the increase in I_D . In general, the origin of EDMR signal is attributed to the recombination process, which is enhanced by flipping triplet into radioactive singlet at spin

resonance. Even though argument could be made in region (i) and (iii) that minor carrier of electrons decreases with the increasing $|V_{GS}|$, and hence less chance for recombination, this argument does not explain the trend shown in region (ii). With the increasing $|V_{DS}|$ chemical potential will increase gradually along the channel, making it easier for other types of carriers entering the material from the side of the channel. Despite the $|V_{DS}|$ induces electrical field dissociating the excitons, a horizontal FET device architecture with channel length of 100um will only provide ~ 0.1 meV energy difference on the feature size of exciton, which is much less than the electron-hole interaction energy. Therefore, there must be a difference origin of the EDMR signal.

To explain the variation of $\Delta I/I_D$ in region (i)-(iii), a spin blocking explanation from bipolaron formation was proposed, followed the work of ref ⁶. As illustrated in Figure 3 (a), some carriers are trapped within some band tail states in the percolation pathways for the mobile carriers. With the applied external field H (perpendicular to the film), both mobile carriers and trapped carriers have a well-defined spin in same direction. When the mobile carriers approach the trap site, it is not allowed to occupy the same trap state due to the Pauli exclusion principle. Instead, they hop to a higher energy state and continue their motion without interference with the trapped charge. At resonance condition, however, the spin of either charge is flipped so that a lower energy state is made available for both charge dwell at same trap, and hence the formation of bipolaron. In other words, the flip of spin turns some mobile charges into trapped ones and hence block its motion. With the more negative V_{GS} in linear and saturation regime, increased Fermi level makes more percolation pathways available, therefore the total current is less prone to this “the trap states” alongside the pathways. During the transition from linear to the saturation regime, the increased drifting current changes the slope of the conduction pathways, making it easier for the charge to “tunnel” through the energy barrier, and hence decreases $\Delta I/I_D$.

Estimation of energy scale and wavefunction expansion with the presence of charge-charge interactions

Following the spin blockade explanations, we then extend the discussion of measurement results to higher temperature for deeper insights of energy scale in bipolaron formation. For DPPDTT, the I_{EDMR} peak is observable in a wide range of temperature from 200K-300K, with the strong bias at p-type linear and saturation region. Normalized current peak $\Delta I/I_D$ decays exponentially with increased temperature, and can be well-fitted to an exponential function (Figure 2 (e))

$$\frac{\Delta I}{I_D} = \tilde{I}_0 \exp\left(\frac{\Delta E_c}{k_B T}\right) \quad (1)$$

with $\Delta E_c = 175$ meV. As previously discussed, the tunnelling effects of the barrier is largely suppressed in linear region with lower drifting voltage, and thermal activation becomes the main driving force for the carrier to overcome the spin blockade barrier. Therefore it is reasonable to assume the extracted activation energy ΔE_c corresponds to the energy barrier induced by the spin blockade, i.e. the energy gap between the ground states and the 1st excited states. This extracted value matches with the prediction of ~ 200 meV energy difference⁶. We first address the importance of coulomb interactions in the energy level separation, as organic semiconductors are widely-acknowledged for their poor electrostatic screening, with relative permittivity $\epsilon_r \approx 3.5$ ¹².

We modelled the formation of bipolarons by double charge carriers (holes) in a single 2D quantum dot by finite elements method (illustrated in Figure 3 (a)). In the transport process with a trapped charge in the pathway, a mobile charge first tries “hopping” to the trapped site to form a temporary

bipolaron states, then hops to a new unoccupied site for further movements. ΔE_c is the energy difference between the ground state (a singlet state S_0) and the 1st excited state (triplet state T_1). In the model, the dimension of 2 reflects the case that the charge is much more mobile for in-plane transport (along the backbone or via the pi-pi stacking) compared with the motion at out-of-plane direction¹³. The simulation suggests that the coulomb interaction is less significant compared with the energy difference between S_0 and T_1 states in the range of energy level we are interested in (as shown for the 2 lowest energy levels in Figure 3 (b)). However, it reduces the S_0 and T_1 energy level differences and results in modifications in prediction of the dot feature size.

By interpolation to the T_1 - S_0 energy level difference with coulomb interaction, a rough estimation of $L_0 = 1.39nm$ which is roughly length scale of the monomer. Given the semicrystalline phase exhibited by spin-coated DPP-DTT films with crystal domain on >10nm scale, the trapped charges forming bipolaron is likely to dwell at the grain boundaries, where the chain is rotated or tilted to a large angle. Another possibility is the bipolaron is formed “transiently” caused by the dynamics of the backbone. (More details about the simulation could be found in Supplementary information section 8).

Readers may attempt to compare the extracted from EDMR with the activation energy extracted from mobility according to the Arrhenius relation $\mu = \mu_0 \exp\left(-\frac{E_A}{k_B T}\right)$, which is $112 \pm 3meV$ for DPPDTT (Supplementary information section 5). However, we point out that the energy scale extracted from EDMR have different origins from the E_A extracted from mobility data – in EDMR, the energy barrier corresponds to the discrete energy level between T_1 and S_0 states due to the confinement nature of trap sites, whereas mobility data accounts for the energy distribution in the band tail.

The origin of the double peak

We now move our focus to the ambipolar region, where EDMR signal exhibits a double peak feature with opposite sign in amplitudes (Figure 2(b), Supplementary information Section 6). The frequency sweep shows observable peak feature from 7~70kHz (shown in Figure 4 (a)), while the direction of the second peak is always downwards, excluding the possibility of phase shifts as artifact in the lock-in detection. Here we address that the existence of the second peak provides a clue to study the increasing/decreasing trend in I_D at resonance condition. In the lock-in detection mode, the sign of the peak mixed with the relative phase of the response to the modulation, thus determination the amplitude of the sign relies on understanding of its underlying process. The knowledge of two counteractive process double-checks the validity of the bipolaron spin blocking mechanism proposed.

In order to further understand whether double peak occurred in ambipolar region requires both types of carriers, or some certain electric potential distribution in FET devices, we fabricated top-gated FET device with 3mol% F4-TCNQ doped DPPDTT by solution mixing (see Method for details). F4-TCNQ is a typical p-type dopant with 5.1eV LUMO energy¹⁴, and has little impact on the material structure¹⁵ other than increasing the number of conducting holes. The AFM measurements also confirms no significant change in DPPDTT microstructure (Supplementary information Section 9), indicating the configuration of the trap states along percolation paths should not change with the addition of dopants. With the doping applied, no signature of second peak occurs within the range of $30V < |V_{GS}| < 80V$ (Figure 5 (b)). This shows both electrons and holes are involved in the process. At this stage, we can make the argument that the second peak is a result of recombination process,

which is enhanced by triplet-to-singlet transition of electron-hole pairs at magnetic resonance condition. The EDMR peak is then recorded at different range of mw power (and hence the mw field in the centre of the cavity), Figure 5 (b) shows the second peak become dominant at stronger mw field. This is explained by the fact that triplet e-h pairs are more closely associated together, compared with the bipolarons, thus experienced a stronger interaction from the other charge. Therefore a stronger microwave field is required to change its spin states. Figure 5 (d) shows the evolution of the double peak feature with the increasing temperature, the peak corresponds to recombination shows similar amplitude at higher temperatures. Because thermal activation is only on the scale of 25meV, it shows its impacts on overcoming the bipolaron energy level – on the scale of 0.1eV, but still not sufficient to affect the formation of exciton. By knowing the opposite trends between the widely observed bipolaron peak and recombination peak, we are now affirmative that the bipolaron formation at magnetic resonance blocks the charge transport.

Another observation with the doped DPPDTT sample is that EDMR peaks in saturation region decreases, compared to the pristine DPPDTT device. This means the charge induced by doping and gating have exchangeable effect in the increase in choices of percolation paths and reducing the effects of bipolaron formation. However, for the comparison of $\Delta I/I_D$ across different devices, the contact resistance over electrode needs to be considered – as $\Delta I/I_D$ decreases with the drift voltage (Figure 2 (c),(d), region (ii)), presence of contact resistance reduces the voltage applied on channel and hence results in overestimation about the $\Delta I/I_D$ value. Saturation region with $|V_{DS}| = 60V$ is only marginally affects by contact resistance, while linear region suffers more with this issue.

General applicability to different polymer systems

We then repeated the same biasing variation and temperature cw-EDMR measurement on other organic polymers. We selected 2 typical polymers - C₁₆-IDT-BT with amorphous structure and shallow charge traps, and C₁₂-pBTTT with high crystallinity and wide range distribution of trap states in energy scales. The F₄-TCNQ doped DPP-DTT transistor is set as reference sample to ensure that all devices work in p-type region to eliminate the effect of contact resistance.

Shown in Figure 5, the EDMR peaks are observed for all material systems. The $\Delta I/I_D$ follows similar trends in region (i) and (ii) with the increased carrier concentration as well as the increased drifting voltage V_{DS} across the conductive channel. (We point out the abnormal peak for IDTBT at $|V_{GS}| = 80V$, $|V_{DS}| = 15V$ is due to the interference with the gate leakage, leading to a lower estimate in the drain current). This confirms the bipolaron spin blocking phenomenon generally exists in all conjugated polymer systems. pBTTT shows highest $\Delta I/I_D$ level, which could be explained by its rich of band tail states. On the other hand, benefitted with sharp band edge, IDT-BT shows lowest level in $\Delta I/I_D$. The decreasing trend of $\Delta I/I_D$ with $|V_{GS}|$ is comparable with all three polymers, which means the hopping sites are uniformly distributed in energy scale of these polymers such that the increased charges get access to new percolation pathways to the same extent. With the increase in drifting voltage $|V_{DS}|$, deformation of bipolaron is allowed by drift current, therefore the differences in trap states population between polymers, and hence $\Delta I/I_D$ are decreased to a similar level of 10^{-7} .

Temperature dependent data was fitted with exponential function to extract the energy level and wavefunction parameters of each polymers, which is summed up in Table 1. pBTTT shows largest trap site in 1.62nm scale. IDT-BT shows a mild size of trap site, however, as it is a purely amorphous material, the coherent length of the wavefunction on the backbone is considerably long, which

agrees with our previous findings and supports the outstanding charge transport performance of this material.

Discussions

Under the magnetic resonance condition, we can control the formation of bipolaron with spin-polarized carriers. By performing the cw-EDMR detection with various gating conditions, it is evident for the existence of bipolaron spin blocking phenomenon in a wide range of conjugated polymer systems. The formation of spin-blocking polaron reflects the characteristic charge “hopping” picture in organic semiconductors, which naturally forms quantum dots from localized hopping sites. As a quantum phenomenon cannot be explained without consideration of the wavefunction of the carriers, this technique provides information not only on population of trap states, but also the wavefunction expansion on the hopping states. In conjugated polymer systems, the localization of charges could either be permanent (certain size of crystal domains), or transient (the tilts or torsions of the polymer backbones).

With the increased number of charge carriers, more choices of hopping states are available to the charges. Therefore, the measured EDMR peak is less significant compared to the increased current. This effect is observed for both electrons and holes, and for a vast range of materials with different level of crystallinity. Doping induced charges have similar effects as gate induced charges. However, it is worth to note that doping processes may also have effects on the material structure, apart from increasing carrier concentration.

Acknowledgements

We would like to thank S. Schott and R. L. Carey for conducting preliminary research on the Electron paramagnetic resonance technique in organic semiconductors. Especially, Z.W. are grateful for S. Schott who developed the software for automatic control of cw-EPR spectrometer and the cryostats with great robustness under various measurement conditions. Z.W. acknowledges financial support from Trinity College in Cambridge for his Ph.D. study.

Author contributions

Z.W. fabricated the transistor devices and conducted the cw-EDMR experiments, analysis the data, and led the project coordination. I.K. and J.B. assisted in building the experimental set-up, helped in data analysis and interpretation of data. T.M. provided expertise in the cw-EPR spectrometer. GIWAXS measurements were carried out by Z.W. and XX in at Diamond light source (I07 beamline). Z.W. contributed to the writing and editing of the final manuscript, with the intellectual inputs from all authors. H.S. supervised the project.

Methods

Device fabrication

EDMR measurements were performed on top-gate, bottom-contact FET devices with narrow width and elongated length to ensure magnetic coupling while retaining the required total number of spin.

To be compatible with the solution-processed OFETs, 40 mm x 40 mm squares Fused-quartz plates (UQG Optics, FQP-5005) were used with 0.3mm depth pre-cut grooves on the back of the substrate at 3mm spacing. The substrate was cleaned by sonication in Decon90, DI water, acetone, and IPA bath for 10min of each process., followed by 10 min of O₂ plasma ashing. We then used photolithography followed by thermal evaporation of 4nm/20nm Cr/Au layer under 5×10^{-6} mbar vacuum to deposit interdigitated source and drain contacts with a total channel width 243mm and length of 0.1 mm per device. Given our long channel architecture, we measured a lower mobility compared to other reports.

The deposition of the organic films goes as follow.

DPPDTT: 10 g/l solutions of DPPDTT in 1,2-dichlorobenzene(o-DCB) were prepared and heated overnight at 80° C. Without O₂ plasma cleaning, we heated the substrates and glass pipettes also at 80° C for five minutes, then spin-coated the solution onto them at 1400 rpm for 60s. Immediately afterward we place the sample on hotplate at 100° C for 2h to evaporate the solvents, before annealing at 320° C for 20 min, and finally quenching them for 5 min.

F4TCNQ doping: after preparing DPPDTT solutions, 1g/L F4TCNQ solution in o-DCB is prepared and heated for 1h at 70° C. Then the solution is mixed at the required level, and heated at 50° C for another hour before spin coating. The substrate with electrode is plasma treated. The spin coating process is the same as pristine DPPDTT. After spin coating, the sample is heated at hotplate at 100° C for 1h, then annealing at 170° C for 20 min, finally quenching for 5 min.

C12-pBTTT: 10g/L solutions of pBTTT 10 g/l solutions of DPPDTT in o-DCB were prepared and heated for 1 hour at 90° C. The substrate with electrode is plasma treated, then transferred to the glovebox immediately. The solution is spin coated onto the substrate at 1500rpm with 60s, then Anneal at 110° C for 30 seconds before setting up the hotplate temperature at 180° C for 20min annealing. Then the hot plate its turned off and cooled down naturally, while the sample is left on the hotplate until temperature drops below 100° C. This process produces terrace phase pBTTT, which has the highest mobility for pBTTT.

C16-IDT-BT: 10g/L solutions of IDTBT in o-DCB were prepared and heated for overnight at 60° C. Then the film is spin coated by a 2 step process i) 500 rpm, 3s dwell and 3s ramp, ii) 1500rpm 3s dwell and 3s ramp. Then the film is annealed at 110° C for 1 hour.

After OSC deposition, solution of 60 g/L PMMA in orthogonal solvent n-butyl-acetate was then spin-coated with 1400 rpm for 60 seconds on top of the annealed semiconductor layer and then annealed at 90°C for 20 min. The top gate of the OFETs were deposited by thermal evaporation of 30 nm Al film over the active areas under 3×10^{-6} mbar vacuum at very low speed of 0.6Å/s. Finally, the devices were separated into 3*40mm devices at the pre-cut grooves using scalpel by applying gentle pressure on the top of device.

Electrical characterization of FI-ESR devices

The cut device was connected to sample holder and wire-bonded to the electrical pads to create electrical connections. The transfer and output curves of the devices are measured with Keithley 2600 source meter. Both linear and saturation mobility are extracted from the related transfer curves based on the MOSFET equations

$$\mu_{lin} = \frac{L}{W} \frac{1}{C_0 V_{DS}} \frac{\partial I_D}{\partial V_{GS}} \quad (V_{DS} < V_{GS} - V_{th})$$

$$\mu_{sat} = \frac{L}{W} \frac{2}{C_0} \left(\frac{\partial \sqrt{I_D}}{\partial V_{GS}} \right)^2 \quad (V_{DS} \geq V_{GS} - V_{th})$$

Field-induced ESR and EDMR measurements

To perform EDMR measurements, a transistor was attached and to a substrate holder with 3 contact pads soldered to the wires to be connected to the measurement equipment. The source, drain, and gate of the transistor were wire bonded to the pads, before slid into a Wilmad Suprasil EPR tube (Sigma-Aldrich product no. Z5674XX) and sealed under nitrogen. The sample was then loaded into an Oxford Instruments ESR900 cryostat, which was controlled by an Oxford Instruments Mercury iTC. The wires were connected to the home-made integrated differential amplifier to provide V_{GS} and V_{DS} biasing while extracting and amplifying AC components in I_D , of which the electrical diagram shown in Figure 1 (a). Cw-ESR and cw-EDMR measurements were taken on a Bruker E500 spectrometer using a Bruker ER 4122SHQE cavity and an X-band microwave source. and a Keithley 2602b source unit was used to provide biasing condition orders to the home-made amplifier. All measurement tools are computer controlled by the code provided in <https://github.com/OE-FET/CustomXepr>.

For the EDMR scans without specification, the microwave power attenuation is set as 4dB, modulation frequency as 40kHz, modulation amplitude as 3 Gauss. Field width of scanning is set as 50 Gauss with 1024 sampling points. 20 scans were performed and averaged to give the final result.

References

1. Schott, S. *et al.* Polaron spin dynamics in high-mobility polymeric semiconductors. *Nature Physics* 2019 15:8 **15**, 814–822 (2019).
2. Van Schooten, K. J., Baird, D. L., Limes, M. E., Lupton, J. M. & Boehme, C. ARTICLE Probing long-range carrier-pair spin-spin interactions in a conjugated polymer by detuning of electrically detected spin beating. *Nat Commun* (2015) doi:10.1038/ncomms7688.
3. Gorgon, S. *et al.* Reversible spin-optical interface in luminescent organic radicals. *Nature* 2023 620:7974 **620**, 538–544 (2023).
4. Murto, P. *et al.* Mesitylated trityl radicals, a platform for doublet emission: symmetry breaking, charge-transfer states and conjugated polymers. doi:10.1038/s41467-023-39834-2.
5. Tait, C. E. *et al.* Spin–spin interactions and spin delocalisation in a doped organic semiconductor probed by EPR spectroscopy. *Physical Chemistry Chemical Physics* **23**, 13827–13841 (2021).
6. Behrends, J. *et al.* Bipolaron formation in organic solar cells observed by pulsed electrically detected magnetic resonance. *Phys Rev Lett* **105**, 176601 (2010).
7. Haneef, H. F., Zeidell, A. M. & Jurchescu, O. D. Charge carrier traps in organic semiconductors: a review on the underlying physics and impact on electronic devices. *J Mater Chem C Mater* **8**, 759–787 (2020).

8. Bronstein, H., Nielsen, C. B., Schroeder, B. C. & McCulloch, I. The role of chemical design in the performance of organic semiconductors. doi:10.1038/s41570-019-0152-9.
9. Chen, Z. *et al.* High-Performance Ambipolar Diketopyrrolopyrrole-Thieno[3,2-b]thiophene Copolymer Field-Effect Transistors with Balanced Hole and Electron Mobilities. **22**, 25–27.
10. Carey, R. L. *et al.* Spin relaxation of electron and hole polarons in ambipolar conjugated polymers. doi:10.1038/s41467-023-43505-7.
11. Morishita, H. *et al.* Linewidth of low-field electrically detected magnetic resonance of phosphorus in isotopically controlled silicon. *Applied Physics Express* **4**, 021302 (2011).
12. Nikolka, M. *et al.* High-mobility, trap-free charge transport in conjugated polymer diodes. doi:10.1038/s41467-019-10188-y.
13. Fratini, S., Nikolka, M., Salleo, A., Schweicher, G. & Sringhaus, H. Charge transport in high-mobility conjugated polymers and molecular semiconductors. *Nature Materials* **2020 19:5 19**, 491–502 (2020).
14. Méndez, H. *et al.* Charge-transfer crystallites as molecular electrical dopants. *Nature Communications* **2015 6:1 6**, 1–11 (2015).
15. Ghamari, P., Niazi, M. R. & Perepichka, D. F. Controlling Structural and Energetic Disorder in High-Mobility Polymer Semiconductors via Doping with Nitroaromatics. *Chemistry of Materials* **33**, 2937–2947 (2021).

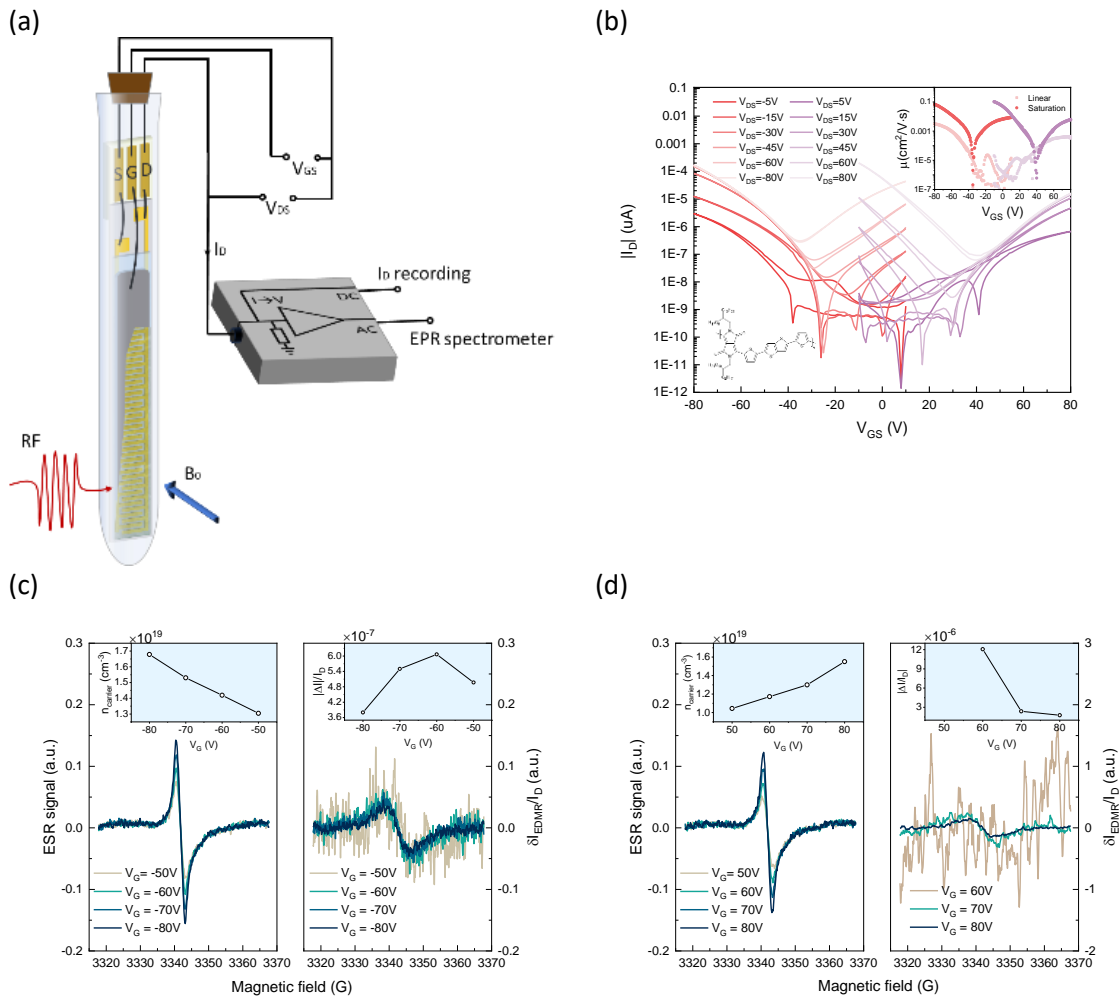


Figure 1 Field-induced cw-ESR and cw-EDMR experiments on ambipolar OFET, (a) Schematic illustration of the experiment, B_0 and RF denote the DC magnetic field and radio-frequency signal applied by EPR, (b) FET transfer curves with balanced p & n type performance, inset is the calculated mobility, (c), (d) EPR / normalized EDMR signal spectra in the p type (hole) linear regime, n type (electron) linear regime, the measured signal is subtracted from a large offset, with is attributed to the eddy current from the circuit loops formed between the device and the external connection wires, inset (shows carrier concentrations and relative change in drain current $\Delta I / I_D$ with gating)

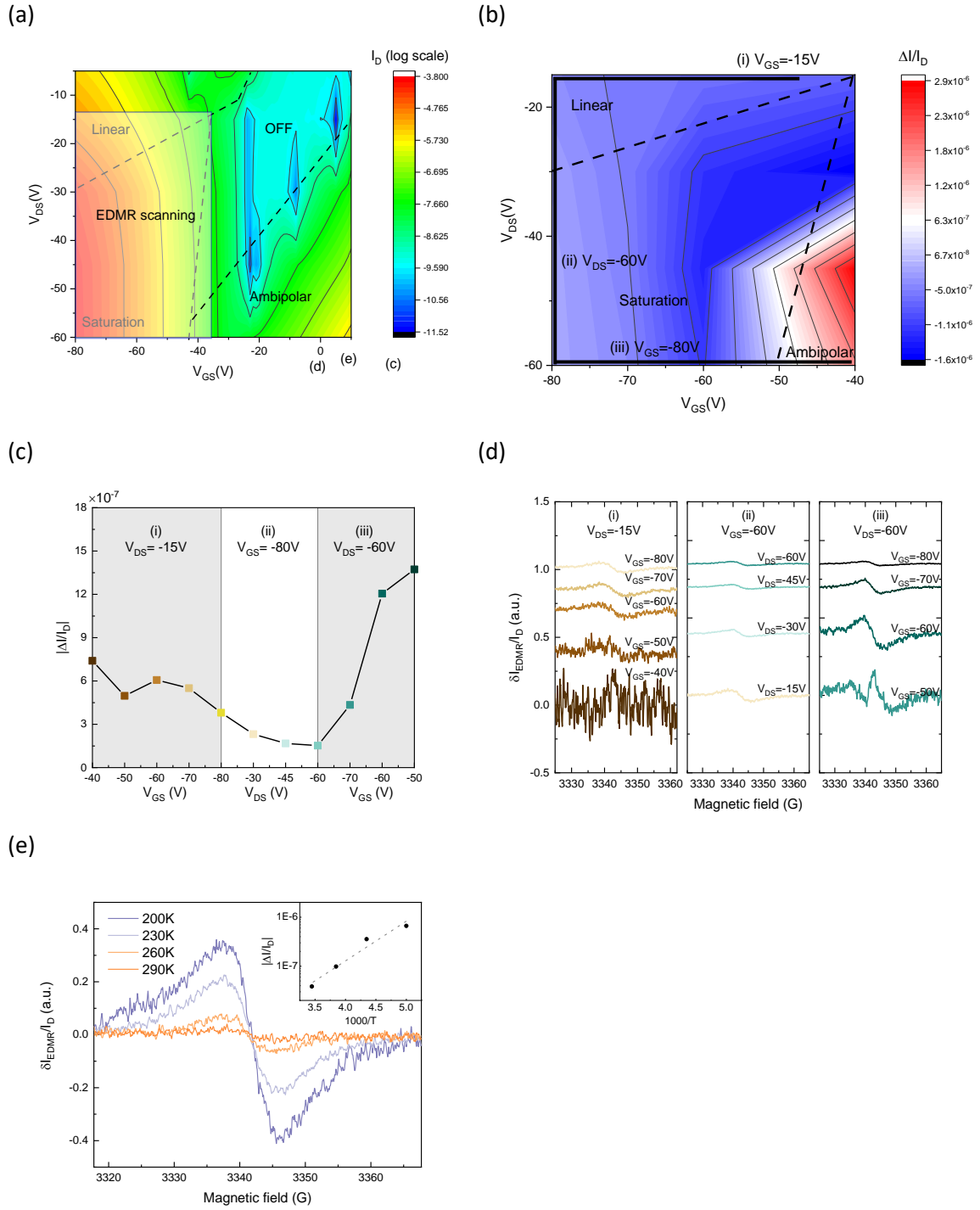


Figure 2 Systematic scan and explanation of origin of the EDMR signal at low temperature, (a) OFET channel current with varying V_{GS} and V_{DS} , with shown systematic detection regime, linear region: a uniform channel with low drifting voltage V_{DS} , saturation region: a channel with decaying carrier density, ambipolar region: a channel with presence of both type of carriers from 2 sides **(b)** the normalized EDMR signal $\Delta I/I_D$ with various combination of V_{GS} , V_{DS} , with the positive and negative area corresponds to their relative signs, **(c)** normalized EDMR $\Delta I/I_D$ with various V_{GS} and V_{DS} followed the routine described in **(b)**, (i) linear region, $V_{DS} = -15V$, $-80V < V_{GS} < -40V$, (ii) linear-to-saturation transition, $V_{GS} = -80V$, $-60V < V_{GS} < -15V$, (iii) saturation region, $V_{DS} = -60V$, $-80V < V_{GS} < -50V$, **(d)** normalized EDMR spectra at the condition corresponding to the data points in **(c)**, **(e)** normalized EDMR spectra measured at linear region $V_{GS} = -80V$, $V_{DS} = -15V$, inset: the exponential fitting of relative peak shift at function of $1000/T$

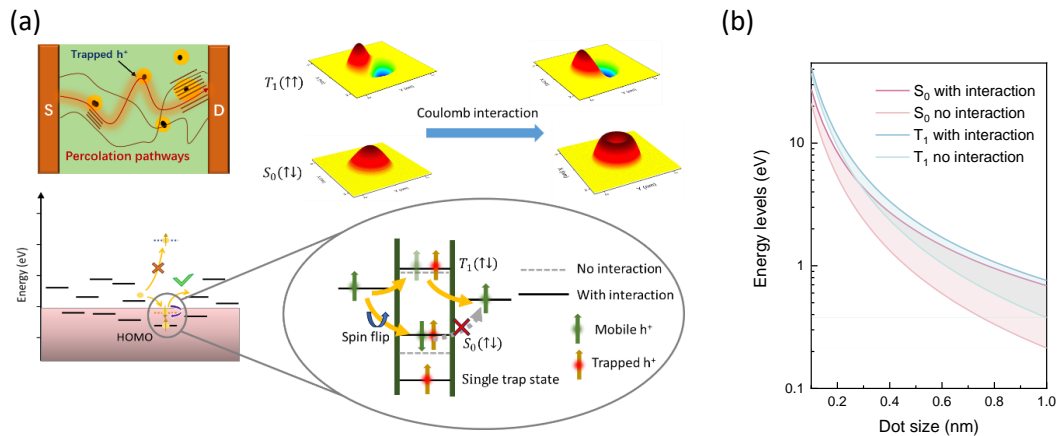


Figure 3 Illustration of the controlled formation of bipolarons under the magnetic resonance condition with presence of Coulomb interactions, (a) a schematic diagram showing the percolation pathways across the multiple crystalline domains, where the mobile charge hops between energetic disordered states, the zoomed in diagrams shows the possible routine a mobile can take when facing a trap site, it can either travel through a higher state with the same spin, or it can flip its spin and dwell at a lower energy level, forming a bipolaron with the charge, the solid and dashed lines show the energy level with/without the Coulomb interactions between charges, respectively, with the wavefunction $\Psi(r)$ corresponding to their relative motion shown, (b) the correction in the 2 lowest energy levels with the presence of Coulomb interaction

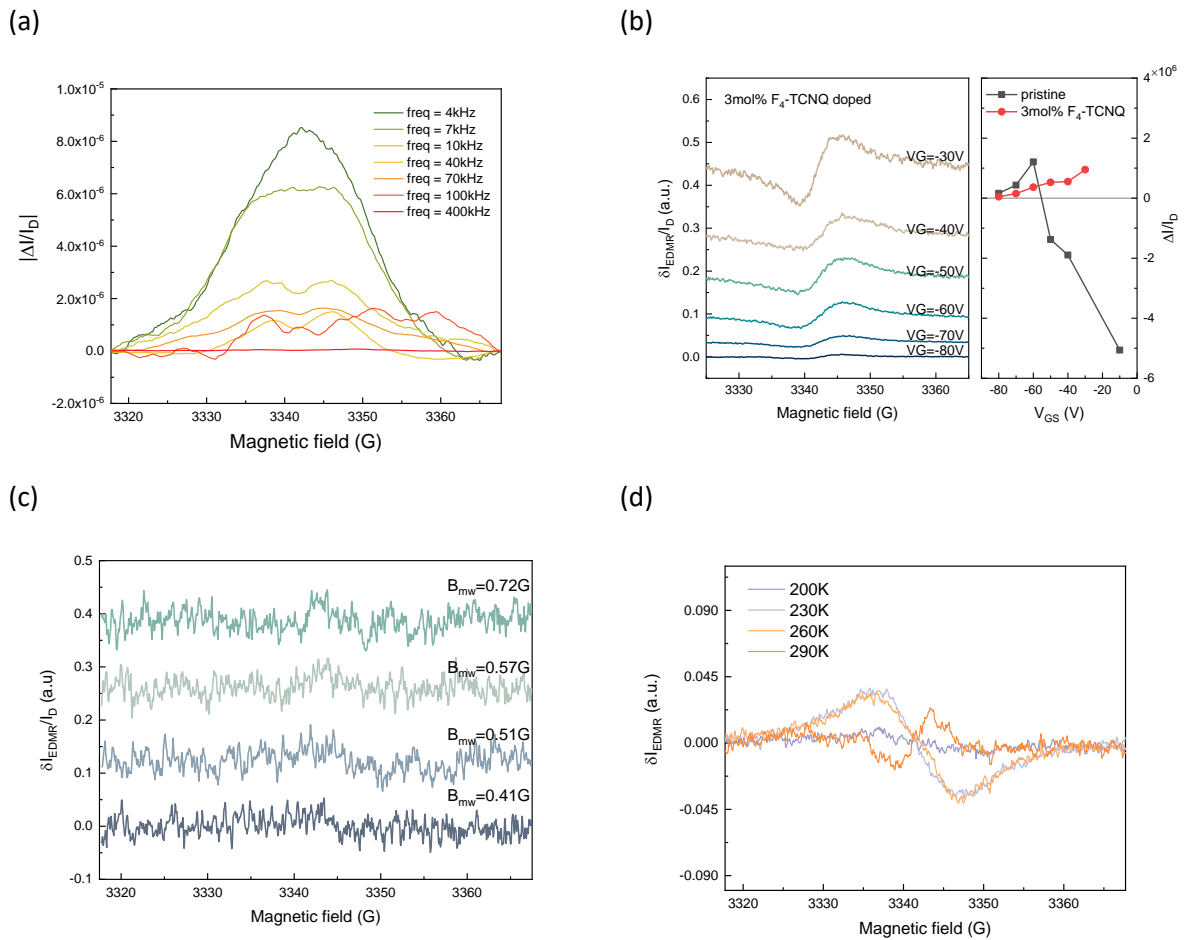


Figure 4 **The presence of the second peak with various changing experimental conditions**, (a) normalized EDMR signal $\Delta I/I_D$ with changing field modulation frequency in ambipolar region $V_{GS} = -30V$, $V_{DS} = -60V$, (b) V_{GS} dependence of EDMR peaks with pristine and F_4 -TCNQ doped DPPDTT transistors in saturation and ambipolar region, (c) normalized EDMR signal $\Delta I/I_D$ with changing microwave power in ambipolar region $V_{GS} = -30V$, $V_{DS} = -60V$, (d) original EDMR data with varying temperature, inset: the normalized EDMR data with varying temperature,

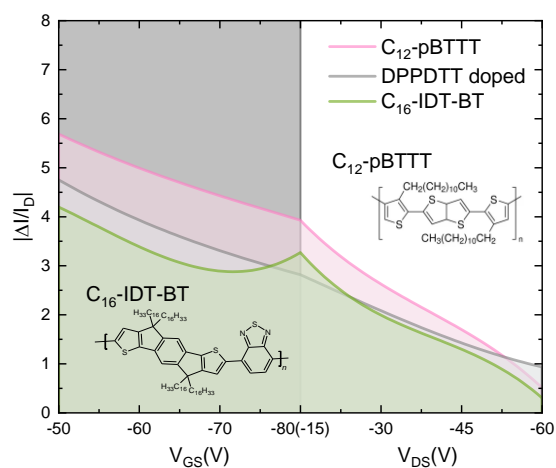


Figure 5 Recorded normalized EDMR $\Delta I / I_D$ at various biasing condition (region (i) and (ii)) for OFET devices C12-pBTTT, F_4 -TCNQ doped DPPDTT, C16-IDT-BT, with the molecular structure of pBTTT and IDTBT shown as inset

Table 1 Extracted saturation mobilities μ_{sat} (representing the bulky transport properties) bipolaron correlation energy, and features size of the trap sites

Polymers	$\mu_{sat} (cm^2 / V \cdot s)$	$\Delta E_C (meV)$	$L_0 (nm)$
C16-IDT-BT	0.399748	132+-34	1.5680
Doped DPP-DTT	0.358862	162+-20	1.4391
C12-pBTTT	0.044370	117+-20	1.6497

Supplementary Information

Controllable bipolaron formation unveiling structural features of trap states in organic charge transport

Zichen Wang¹, Ilia Kulikov², Tarig Mustafa¹, Jan Behrends², Henning Sirringhaus^{1*}

1. Optoelectronics Group, Cavendish Laboratory, University of Cambridge, JJ Thomson Avenue, Cambridge CB3 0HE, UK

2. Berlin Joint EPR Lab, Freie Universität Berlin, Fachbereich Physik, Arnimallee 14, D-14195 Berlin, Germany

*hs220@cam.ac.uk

Contents

1. Determination of dielectric and film thickness of PMMA.....	18
2. Evaluation of device change with continuously applied bias.....	19
3. Gaussian and Lorentzian fitting.....	20
4. Observed cw-EDMR signals and the design of home-made amplifier.	22
5. Estimation of activation energy.....	23
6. Evaluation of data integrity with double peak feature.....	25
7. Effect of B field modulation frequency on the overall EDMR signal	26
8. Modelling of 2D quantum dots	27
9. F ₄ -TCNQ doped DPPDTTs.....	29

1. Determination of dielectric and film thickness of PMMA

The discussion about the normalized EDMR signal of source-drain current $\delta I_{EDMR}/I_D$ on a transistor relies on the assumption that gate leakage current is negligible, usually 10^{-1} in practice. Therefore 50, 60, 80 g/L Poly(methyl methacrylate) (PMMA) in n-butyl acrylate (nBA) solvent was tried, and optimized concentration of 60g/L was finally selected to minimize the gate leakage while maintaining the capacitance of gating. We address the issue that the film thickness diverges from the widely accepted $t \propto \frac{n_{sol}}{\sqrt{\langle spin\ speed \rangle}}$ relationship, and the dielectric constant depends on the film thickness. We used the Bruker DekTak to measure the film thickness. Then we fabricated a trilayer capacitance devices structure of ITO, PMMA film and 30nm Al top electrodes with overlapping area of (3mm*1.5mm). and the Impedance analyser was used to measure the capacitances. Top Al gate is thermally evaporated under $3 * 10^{-6} mBar$ at the rate of $0.7 \text{ \AA}/s$ with shadow mask. 8 top gated devices were fabricated and measured for each PMMA concentration level to account for the measurement error for overlapping area and non-uniformity of the film. The impedance was checked over frequency range of 50Hz~10kHz, while the capacitance value is extracted at 100Hz (the lowest value to extract a value with smooth curve, shown in Figure S1). The extracted parameters for film thicknesses, unit capacitance and dielectric constants were summed up in Table S1. The capacitance value extracted at 50g/L agrees with our previous work¹.

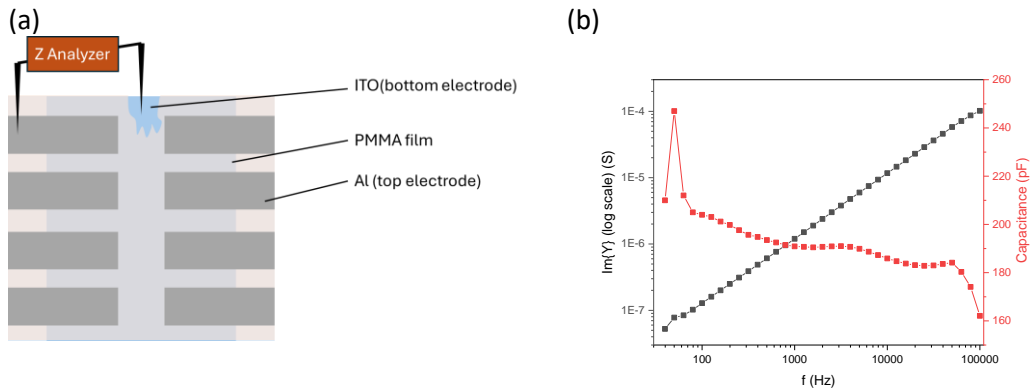


Figure S1 Measurement of dielectric capacitances by trilayer structure (a) layout of 8 capacitor devices and the measurement scheme, (b) the measured imaginary part of admittance (ωC) and the calculated capacitance values as function of frequency

Table S 1 Extracted dielectric film thickness, capacitance per unit area and relative permittivity for different PMMA concentrations

PMMA Concentration	Thickness(nm)	C per unit area ($10^5 F/m^2$)	ϵ_r
50g/L	395.8	5.921	2.646599
60g/L	550.3	5.008	3.112609
80g/L	1205.7	2.046	2.786723

2. Evaluation of device change with continuously applied bias

The cw-EDMR signal is scanned and taken average of 15-20 times, which takes time for 20-30 minutes for each data point. A rising concern is the degradation of sample with long-time biasing. In the measurement, we set up a recover time of 1h such that the device is in a similar condition after changing bias or temperature. Figure S2 shows the time evolution of drain current I_D and mobility (which is regards as indicator of the trap states) of pBTTT and IDT-BT FETs under 30min biasing followed by 1h recover time. This will allow readers to evaluate stability in range of high-crystalline material to amorphous ones under room temperature. After 2-3 cycles, the devices exhibit repeatable manner, therefore we justified that the $\delta I_{EDMR}/I_D$ value extracted by sequential change of bias condition is comparable. We took average value of the drain current for normalization of I_{EDMR} signal. Figure S3 shows the real time sequence of measurement steps, it is also note worthy that the degradation is less significant when taking measurements at lower temperatures, therefore the recovery time could be slightly shortened.

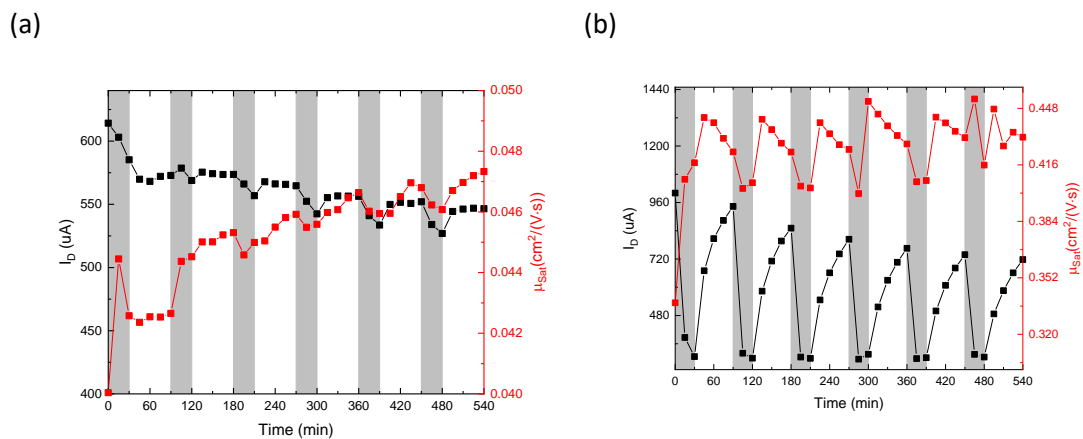


Figure S2 The time evolution of the drain current I_D and saturation mobility μ_{sat} with the applied measurement scheme of 30min stress and 60min recovering time, OFET made from (a) pBTTT and (b) IDT-BT

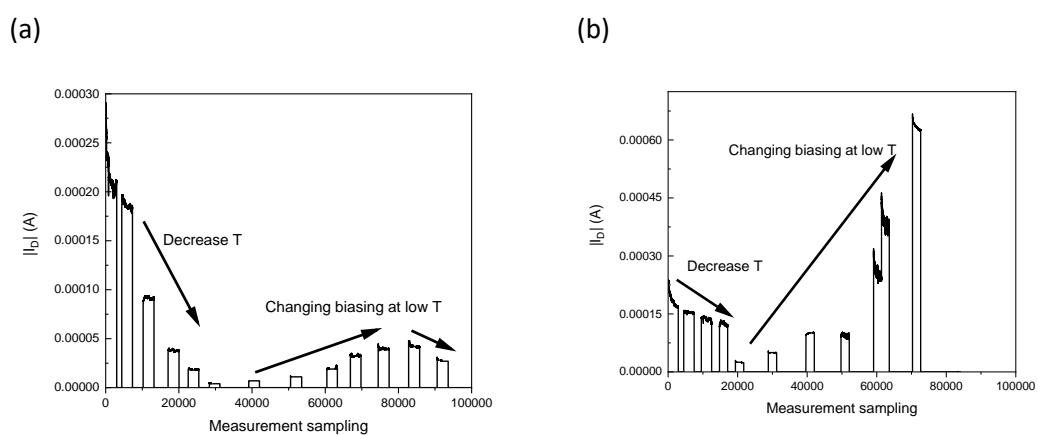


Figure S3 The real time recorded drain current I_D of (a) pBTTT and (b) IDT-BT OFET, the first 4 peaks is taken at 290K, 277K, 245K, 220K, respectively, while other peaks are taken at 200K with various biasing conditions

3. Gaussian and Lorentzian fitting

It is natural to think about the lineshape of the wavefunctions inspired by S Schott et.al, in order to evaluate the level of carrier localization. Figure S4 shows the fitting results of pristine DPPDTT transistor biased at $V_{GS} = -(+)80V$, $V_{DS} = -(+)15V$ at temperature of 200K, corresponding to a typical situation at p(n) linear region. The Lorentzian function only shows marginally improved performance in fitting (Table S2), which makes it difficult to draw conclusion about the origin of the linewidth broadening – it can either be some short lifetime in the transport process or the inhomogeneity in chemical environments experienced by the trapped charges. We first pointed out that the EDMR and the field-induced ESR detects different lifetimes of carriers – ESR picks-up the spin dephasing lifetime, while EDMR corresponds to the correlation function of elementary currents from well-defined carrier states – and hence it is not surprising that EDMR detects much shorter lifetimes given that charge transport takes incoherent manner of “hopping”. Lorentzian fitting of the temperature-dependent EDMR data gives a consistent width over temperature (shown in Figure S5), which conflicts with the motional narrowing explanation. Therefore, we make the argument that EDMR reflects the nature of charge localization around the trap states.

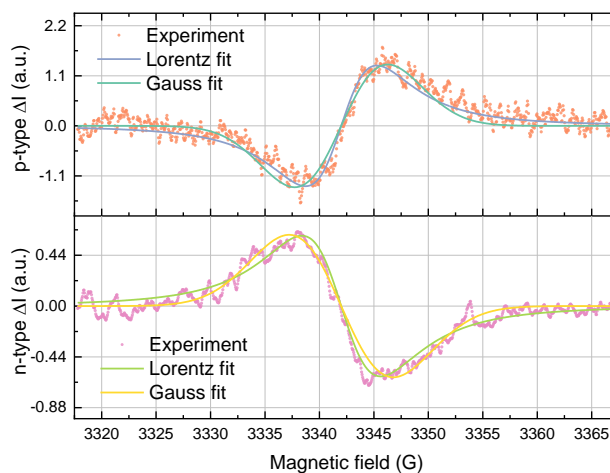


Figure S4 Measured EDMR peaks with Gaussian and Lorentzian fits at p and n type linear region $V_{GS} = -(+)80V$, $V_{DS} = -(+)15V$

Table S2 Residual standard derivation $S_{res} = \sqrt{\sum(y_i - y_{fit,i})^2 / (N - 2)}$ of fitting

Fitting method	Lorentzian	Gaussian
P-region	0.186791	0.210593
N-region	0.06877	0.068954

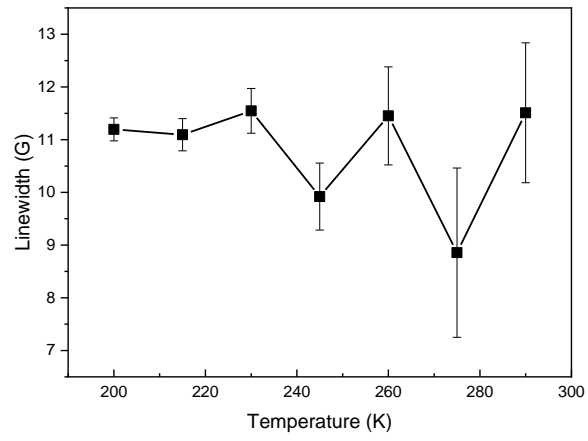


Figure S5 Lorentzian fit of the EDMR peak linewidth at various temperature in p-type linear region $V_{GS} = -80V$, $V_{DS} = -15V$

4. Observed cw-EDMR signals and the design of home-made amplifier.

The lock-in detection scheme of the cw-EDMR works by modulating DC magnetic field and allowing the transistor current I_D to change with B_0 according to the current peak at resonance condition. The I_D variation is then recorded and correlated with the B_0 modulation, to give output spectrum proportional to $\frac{dI}{dB}$. In ideal case, the response of I_D should be in-phase. However, the change in B_0 also induces some eddy current, namely Faraday current, in the conduction loop formed between FET and the amplifier circuits. Therefore, the measured EDMR spectrum always in superposition with a large bias. It is noteworthy that the phase of the Faraday current could be different from the EDMR response, and the sign of the EDMR response cannot be obtained by directly observing the EDMR spectrum.

The measured EDMR signal is in arbitrary unit after process from the home-made amplifier and the EPR build in lock-in amplifier. However, with the Faraday current as reference, the changes in I_D could be estimated. The home-made amplifier first converts the change in I_D into voltages with certain conversion ratio α_{IV} then decouples the AC components from DC values. By feeding the AC component of I_D into a microscope off the resonance, the peak-to-peak value of the Faraday loop V_{pp} could be measured. It corresponds to the readings in the spectrum

$$V_{pp} = k \cdot \mathcal{R} \quad (S2)$$

Assuming the linear response of the amplifier, the changes in spectrum readings due to EDMR peaks converts into

$$k \cdot \delta\mathcal{R} = \delta V_{pp} = \alpha_{IV} \frac{dI_D}{dB} \cdot 2\Delta B_0 \quad (S3)$$

. The factor of 2 is the difference between the peak-to-peak value in calculation and the modulation amplitudes set in EPR apparatus. With this simple calibration, the changes in I_D at resonance condition could be calculated by integrating the measured spectrum multiplied by a factor of $\frac{V_{pp}}{2\mathcal{R}\alpha_{IV}\Delta B_0}$. In measurement, it should be kept in mind that α_{IV} is frequency dependent and the value should be compensated based on the frequency response function of the amplifier/filter.

5. Estimation of activation energy

It is intuitive to compare the energy level increment induced by spin blockade mechanism with the activation energy in disordered polymer systems. Transfer curve of the FET was measured in temperature range between 200K to 290K, with the same device in the ESR cavity for cw-EDMR measurements. The linear mobility μ_{lin} was then calculated and the activation energy E_A was calculated by fitting to the equation

$$\mu_{lin} = \mu_0 \exp\left(-\frac{E_A}{k_B T}\right) \quad (S4)$$

, with Boltzmann constant k_B .

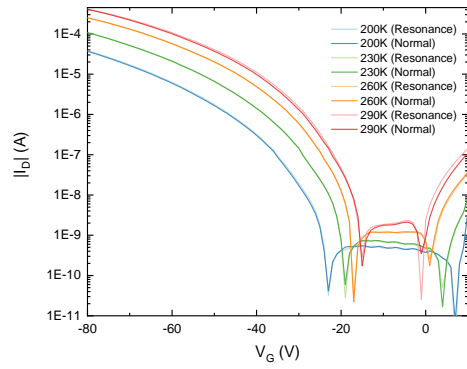
In our measurements, the device was kept in ESR cavity, the microwave power was always turned on to maintain same level of possible heating to the cavity. 4 transfer curves were recorded in 2 conditions: 1) the DC magnetic field switched off, 2) DC magnetic field is applied at resonance condition. In each condition, transfer curves were taken both when the temperature is increasing and decreasing, in interweaving manner as shown in Table S3. It is to exclude any systematic differences in temperature.

Table S3 Sequence of temperature-dependent characterization measurements at resonance/non-resonance conditions

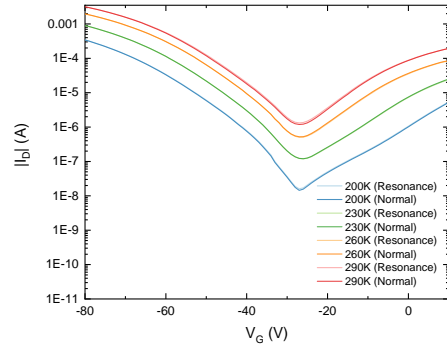
Measurement order	Resonance condition	Temperature condition
1	at resonance	Decreasing
2	off resonance	Increasing
3	off resonance	Decreasing
4	at resonance	Increasing

The extracted linear mobility μ_{lin} follows a good exponential relationship with $1/T$, as shown in Figure S6. No significant difference in transfer curve was observed at different resonance conditions, compared with the error of the fitting. The activation energy was extracted as $112 \pm 3 meV$. This result indicates the energy level shift induced by spin blockade mechanism is small compared to the energy level disorder.

(a)



(b)



(c)

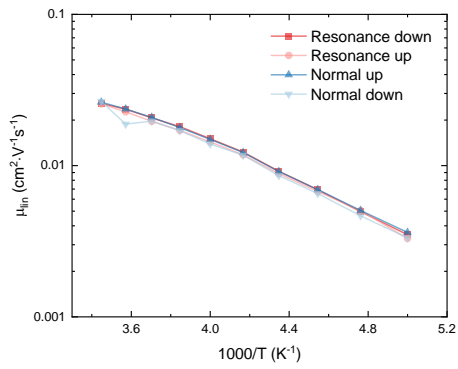


Figure S6 **Temperature dependence of transfer curves of OFET devices under resonance or non-resonance conditions**, transfer curve in (a) linear regime, (b) saturation regime measured at various temperature, (c) extracted linear mobilities changes with temperature at resonance or non-resonance conditions

6. Evaluation of data integrity with double peak feature

At the resonance condition, especially at the condition with the second peak feature, there could be a concern about the effect of changed impedance on signal. With the increased impedance of the FET channel, the total RC time constant $\tau = R_{tot}C_i$ of the circuit formed between OFET device and the amplifier could be changed. It has 2 sequences, i) it could change the phase of the measured EDMR signal and the measured second peak from each channel might be a result of phase shift (illustrated in Figure S7 (a)); ii) RC time constant change cause additional filtering effect and the signal amplitude is not well-estimated. Despite calculating the amplitude of the signal solves the problem i), the problem ii) is still not addressed. Here we calculated the relative phase as a function of external B field. Figure Figure S7 (b) (c) shows the phase shift is negligible. This addressed problem i) and ii) simultaneously, because the change of RC time constant must be accompanied with a phase shift. It is then concluded that the change in impedance is neglectable. After application of a rotation of phase of -139.27° for the whole spectrum, all difference in amplitude presents on the real axis.

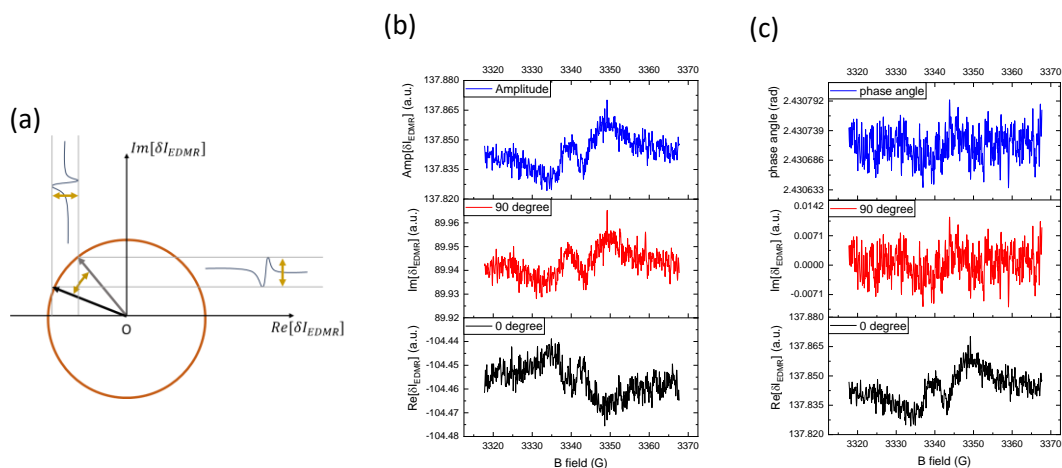


Figure S7 **Illustration of the effect of phase**, (a) the effects of phase shift at resonance condition may have on the recorded amplitude, the recorded EDMR data at in-phase and 90-degree channel (b) before and (c) after applying phase rotation

7. Effect of B field modulation frequency on the overall EDMR signal

The cw-EDMR signal of FI-ESR device in linear regime was recorded at different magnetic field modulation frequencies between 1kHz and 400kHz at 200K in searching for the optimized measurement conditions, shown in Figure S8. The signal first increases then decreases in exponential manner, following the response of the home-made amplifier. The operating B field modulation frequency is chosen to be 40kHz for the best signal to noise ratio.

Phase difference at EDMR peak position is observable at low frequency below 10kHz. This indicates the EDMR signal was not at same phase as the Faraday current, which could be a result from the RC time constant as described in Section 6.

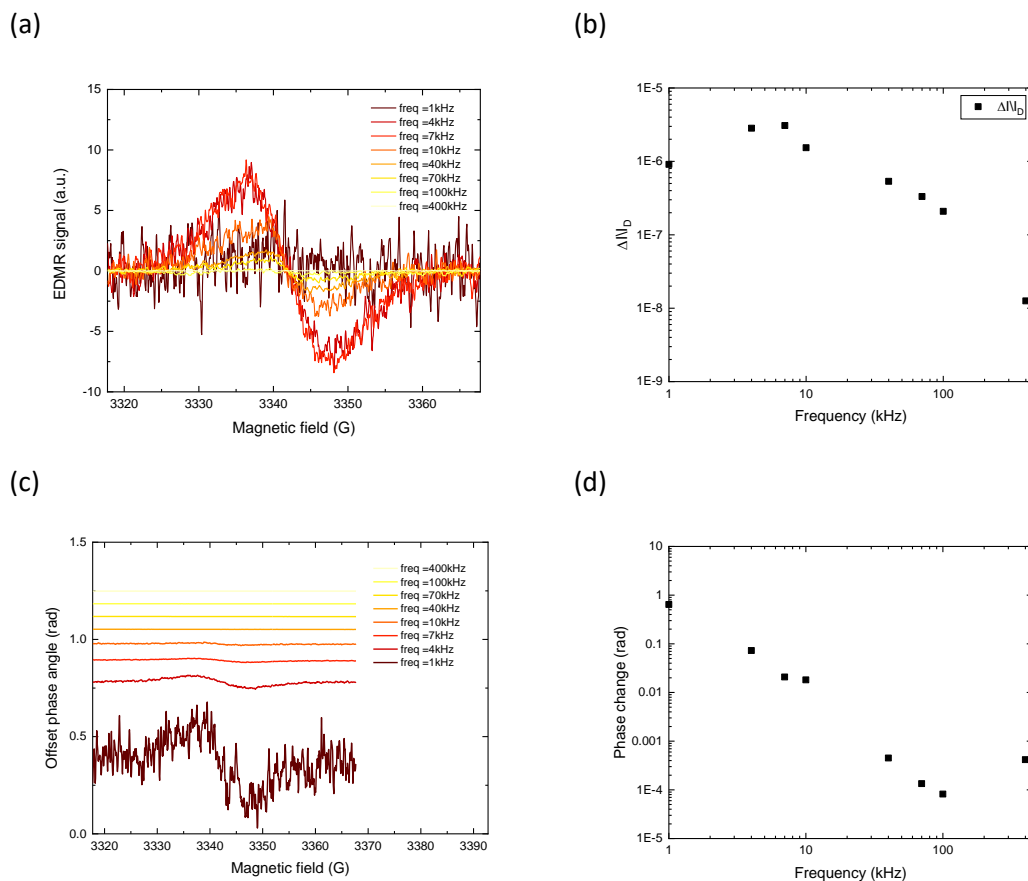


Figure S8 cw-EDMR peak responses with various modulation frequency of applied magnetic field ΔB , changes of cw-EDMR (a) waveforms, (b) peak amplitudes, (c) relative phase, (d) max phase difference with different frequencies

8. Modelling of 2D quantum dots

The quantum dot with the presence of 2 charge carrier is characterized by its Hamiltonian

$$H = -\frac{\hbar^2}{2m_e}(\nabla_{r_1}^2 + \nabla_{r_2}^2) + \frac{1}{4\pi\epsilon_0\epsilon_r} \frac{e^2}{|r_1 - r_2|} \quad (S5)$$

. With the transformation of coordinates, equation (2) is derived. We refer to MATLAB partial differential solver toolbox for simulation, following a general sequence of i) create model, ii) defining geometry, iii) specify equation parameters, iv) generate mesh, v) solving PDE eigenvalue problem. The finite element method is preferred than finite difference method to have a better evaluation around the pole at origin. For the ease of simulation, the Hamiltonian is reduced to

$$H_{Rel} = -\nabla_r^2 + \frac{1}{\epsilon_r|r|} \quad (S6)$$

$$H_{CoM} = -\nabla_R^2$$

The effect of the reduction only changes the units of coordinates as Bohr radius a_B and the energy scale of the output eigenvalue as Rydberg constant R_y . The overall energy should be calculated by

$$E_{tot} = 2 * E_{Rel} + \frac{E_{CoM}}{2} \quad (S7)$$

, where E_{Rel} and E_{CoM} are the eigenvalue from the equations (S5) (S5)(S6), (S5)(S5)(S5) respectively.

The geometry for the simulation is defined as a circle $R = L_0/2$ and together with $\frac{1}{4}$ circle coincide at centre. The purpose of this is to add one vertex exists at centre, so that the mesh could be set to a small step at centre. As the potential reaches infinitely with the speed of $1/r$, mesh goes to a minimal size $\delta = 10^{-4}$. We set Dirichlet boundary condition as $\Phi|_{r=L_0/2} = 0$. Other parameters are set as default. The equation solver will give the eigenvalues and eigenfunctions of the equation (we set the initial range for finding parameters to be [0 5]).

For further details about model implementation, we refer to the MATLAB documentation at <https://uk.mathworks.com/help/pde/pde-problem-setup.html>.

The 1 D simulation is implemented by an ordinary equation solver employing finite difference method, followed by i) defining Hamiltonian matrix and ii) diagonalization steps. The model length range is set as $-\frac{L_0}{2} < z < \frac{L_0}{2}$ with 10000 steps. The potential $V(r) = \frac{1}{\epsilon_r|r|}$ is set as maximum value of 10000. We plot the energy difference between S_0 and T_1 states against $1/L_0^2$, which shows divergence from the non-interactive case with increased dot size. The energy levels of charges without the presence of interactive has an analytical solution as

$$E_n = \frac{n^2\hbar^2\pi^2}{2m_eL_0^2} = n^2 \left(\frac{\pi a_B}{L_0}\right)^2 \quad (\text{in Rydberg}) \quad n = 1,2,3 \dots \quad (S8)$$

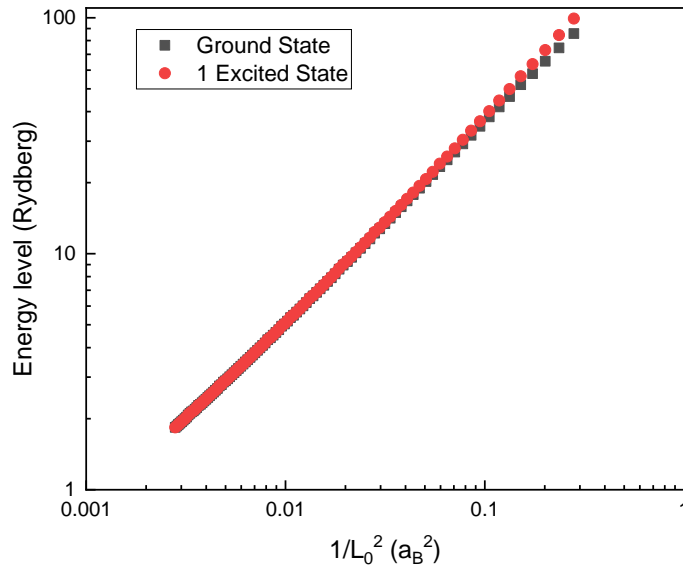


Figure S9 Plot of lowest 2 energy levels with respect to $1/L_0^2$ for simulation in 1D case

Finally we clarify that the purpose of the simulation based on the circular quantum dot “toy model” is not to have a precise estimation of the carrier configuration on the backbone, but to estimate the energy scale of coulomb interaction and then estimate a length scale of localization to help understanding its underlying physics. In real 3D case, the coulomb interaction is further relaxed by the carrier adjusting position to avoid each other on the 3rd dimension. More accurate density-functional-theory based simulation with isolated several repeat units could be used to evaluate the level of backbone tilting or rotation, which will unveil the material parameters not obtainable by X-ray scattering. However, this is beyond the scope of this article for the discussion about the bipolaron spin blocking phenomenon.

9. F₄-TCNQ doped DPPDTTs

To compare the doped DPPDTT devices with other p-type polymers, the reader may be interested to evaluate the impact of the dopant on the material structure itself. Here we present AFM images for a comparison study on pristine DPPDTT films with 3mol% and 5mol% doping levels. The surface morphologies of the pristine and 3 mol% samples are similar, in contrast to that of 5 mol%, where small particles are observed and the film is more homogeneous in the absence of micro-structures as found in its counterparts.

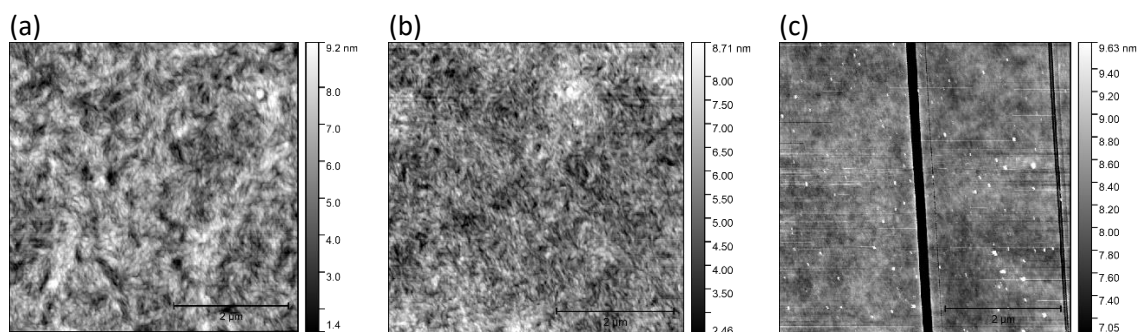


Figure S 10 The AFM images of the film morphology of (a) pristine DPPDTT, DPPDTT with (b) 3mol% and (c) 5mol% F₄-TCNQ doping